

24 **Abstract.** Detailed knowledge of vegetation structure is required for accurate modelling
25 of terrestrial ecosystems, but direct measurements of the three dimensional distribution
26 of canopy elements, for instance from LiDAR, are not widely available. We investigate
27 the potential for modelling vegetation roughness, a key parameter for climatological
28 models, from directional scattering of visible and near-infrared (NIR) reflectance
29 acquired from NASA's Moderate Resolution Imaging Spectroradiometer (MODIS). We
30 compare our estimates across different tropical forest types to independent measures
31 obtained from: (1) airborne laser scanning (ALS), (2) spaceborne Geoscience Laser
32 Altimeter System (GLAS)/ICESat, and (3) the spaceborne SeaWinds/QSCAT. Our
33 results showed linear correlation between MODIS-derived anisotropy to ALS-derived
34 entropy ($r^2= 0.54$, $RMSE=0.11$), even in high biomass regions. Significant relationships
35 were also obtained between MODIS-derived anisotropy and GLAS-derived entropy
36 ($0.52 \leq r^2 \leq 0.61$; $p < 0.05$), with similar slopes and offsets found throughout the season,
37 and RMSE between 0.26 and 0.30 (units of entropy). The relationships between the
38 MODIS-derived anisotropy and backscattering measurements (σ^0) from
39 SeaWinds/QuikSCAT presented an r^2 of 0.59 and a RMSE of 0.11. We conclude that
40 multi-angular MODIS observations are suitable to extrapolate measures of canopy
41 entropy across different forest types, providing additional estimates of vegetation
42 structure in the Amazon.

43

44 **Keywords:** canopy roughness, multi-angle, MODIS, MAIAC, LiDAR, anisotropy

45

46

47 **1. Introduction**

48

49 Terrestrial vegetation plays a significant role in the re-distribution of moisture and
50 heat in the surface boundary layer, as well as in the energy balance of the planet
51 (Bastiaanssen et al., 1998a). Land-atmosphere interactions are driven by the three-
52 dimensional structure of vegetated land cover, including surface roughness, leaf area
53 and canopy volume (Vourlitis et al., 2015; Domingues et al., 2005). Canopy roughness,
54 defined as vertical irregularities in the height of the canopy (Chapin et al., 2011), plays a
55 key role in earth system modelling. For instance, evapotranspiration is controlled much
56 more by canopy roughness (and therefore aerodynamic conductance) than by canopy
57 leaf area or maximum stomatal conductance (Chapin et al., 2011).

58 At stand level scales, significant advances have been made measuring canopy
59 vegetation structure from Light Detection and Ranging (LiDAR). LiDAR allows direct
60 measurements of the three-dimensional distribution of vertical vegetation elements from
61 ground-based (Strahler et al., 2008), airborne (Wulder et al., 2012) and orbital platforms
62 (Sun et al., 2008). To date, most vegetation related LiDAR applications rely on airborne
63 platforms for data acquisition, with measurements acquired at altitudes between 500 and
64 3000 m (Hilker et al., 2010). Due to cost and practical considerations, the availability of
65 airborne LiDAR is currently limited to specific research sites and data are not available
66 across the landscape.

67 The Geoscience Laser Altimeter System (GLAS), onboard the Ice, Cloud, and land
68 Elevation Satellite (ICESat), has provided certain capability to map vegetation
69 characteristics across broader areas from space (Zwally et al., 2002). GLAS is a large-
70 footprint, waveform-recording LiDAR that measures the timing and power of the 1064
71 nm laser energy returned from illuminated surfaces (Schutz et al., 2005). **While not**
72 **configured for vegetation characterization, the GLAS instrument allows quantification**

73 of the vertical distribution of plant components relative to the ground over vegetated
74 terrain (Harding, 2005; Yu et al., 2015, Morton et al., 2014). GLAS data has been
75 successfully used to discriminate forest structure across various biome types (Boudreau
76 et al., 2008; Gonçalves, 2014; Lefsky et al., 2005; Pang et al., 2008) and to estimate
77 canopy light environments and forest productivity (Stark et al., 2014; Rap et al., 2015;
78 Morton et al., 2016). While GLAS provides larger spatial coverage, its footprint is still
79 spatially discrete and importantly a lack of repeated measurements prevents its use for
80 estimation of climate related responses of vegetation.

81 Perhaps complimentary to structural observations, optical remote sensing available
82 from satellite data, provide global coverage at frequent time steps but can generally not
83 deliver accurate information on the vertical organization of plant canopies. For instance,
84 vegetation indices provide general information on canopy “greenness” but their ability
85 to detect changes in high-biomass areas is limited due to a well-documented saturation
86 effect (Carlson and Ripley, 1997). Although VIs have been employed as proxies for
87 vegetation structure, including roughness lengths for turbulent transfer, field estimates
88 of vegetation structure attributes are often only moderately correlated with VIs and their
89 derivatives (Glenn et al., 2008).

90 As an alternative to conventional, mono-angle observations, the combination of
91 multiple view angles may provide new opportunities for modelling the structure of
92 vegetated land surfaces (Breunig et al., 2015; Shaw & Pereira, 1982) from optical
93 remote sensing. Changes in canopy structure including changes in tree crown size,
94 shape, density and spatial distribution of leaves, affect the directional scattering of light
95 (Chen et al., 2005). Multi-angle observations of this scattering may therefore allow us to
96 describe the three-dimensional structure of vegetation (Chen and Leblanc, 1997;
97 Strahler & Jupp, 1990). Multi-angular scattering of surface reflectance (anisotropy) has

98 been linked to optical properties and geometric structure of the target (Widlowski et al.,
99 2004; Widlowski et al., 2005), including canopy roughness (Strahler, 2009), leaf angle
100 distribution (Roujean, 2002), leaf area index (LAI) (Walthall, 1997) and foliage
101 clumping (Chen et al., 2005; Chopping et al., 2011). Such estimates may even be made
102 in dense canopies (Moura et al., 2015), as observations acquired from multiple view
103 angles decrease the dispersion and saturation effect in geometrically complex vegetation
104 (Zhang et al., 2002).

105
106 With the advent of multi-angular sensors such as the Multi-angle Imaging
107 SpectroRadiometer (MISR) (Breunig et al., 2015) and POLDER (Roujean, 2002), the
108 dependence of reflectance on observation angles has been documented (Barnsley et al.,
109 2004) and modelled (Roujean et al., 1992; Wanner et al., 1995). Recent progress using
110 the Multi-Angle Implementation of Atmospheric Correction Algorithm (MAIAC) has
111 allowed the acquisition of multi-angle reflectance across large areas and at high
112 observation frequencies by combining satellite imagery obtained from NASA's
113 Moderate Resolution Imaging Spectroradiometer (MODIS) Terra and Aqua platforms
114 during a few overpasses (Lyapustin et al., 2012a; Moura et al., 2015). Such observations
115 could potentially allow periodic and spatially contiguous estimates of vegetation
116 structure and its response to changes in climate variables. When correlated with more
117 direct measurements of canopy structure by other instruments, such as LiDAR, this may
118 then allow us to extrapolate canopy roughness and other structural estimates in space
119 and time, thereby filling key data gaps for improving our understanding of ecosystem
120 structure and functioning. Further validation may be provided by scatterometer
121 observations over dense forests. For instance, the SeaWinds microwave radar, onboard
122 NASA's QuikSCAT satellite, was primarily designed to measure near-surface wind
123 speed and direction over the oceans. However, due to its high sensitivity to water

124 content that drives canopy dielectric properties, it has been also used to study canopy
125 structure (Frolking et al., 2011; Saatchi et al., 2013).

126 In this study, we used estimates of canopy roughness obtained from 1) airborne
127 laser scanning (ALS), 2) spaceborne LiDAR GLAS, and 3) the spaceborne SeaWinds
128 scatterometer, to evaluate the potential of multi-angular MODIS observations for
129 modelling vegetation roughness from directional scattering of visible and near-infrared
130 (NIR) reflectance. We implemented a spatial scaling approach, from airborne to orbital
131 levels of data acquisition, to model continuous coverage of roughness across tropical
132 forests of the Xingu basin area in the Brazilian Amazon. Our objective was to test
133 whether multi-angle MODIS reflectance can be used as a proxy for canopy roughness
134 over Amazonian tropical forests, including different forest types such as Dense and
135 Open ombrophilous Forests, and Semi-Deciduous Forest.

136

137 **2. Methods**

138 ***2.1. Study area***

139 The study area is located in the southeast part of the Amazon, including the Xingu
140 basin and adjacent areas (Figure 1). Figure 1 also shows the GLAS transects for the
141 study area (Schutz et al., 2005) as well as the ALS and the field data plots. The study
142 area presents a south-north gradient with respect to climate. Following the Köppen
143 classification, the southern portion of the study area is dominated by tropical wet and
144 dry climate (Aw), while the north portion is characterized by tropical monsoon climate
145 (Am). Length and duration of the dry season, defined as months with rainfall less than
146 100 mm or less than one third of precipitation range (Asner & Alencar, 2010; Myneni et
147 al., 2007), also varies across the study area. In the southern parts, the dry season lasts
148 about five months, from May to September (Moura et al., 2012). In the northern parts, a

149 drier climate prevails between July and November (Vieira et al., 2004). The area is
150 characterized by three predominant forest types: Dense Ombrophilous Forest (Dse),
151 Open Ombrophilous Forest (Asc) and Semi-Deciduous Forest (Fse) (IBGE, 2004).

152

153 **(Figure 1)**

154

155 ***2.2. Field inventory data***

156 Estimates of vegetation structure were derived for each of the three different forest
157 types using available inventory plots across the region. For two vegetation types, Open
158 Ombrophilous Forest (Asc) and Semi-deciduous Forest (Fse), surveys were provided
159 by the Sustainable Landscapes Brazil project in collaboration with the Brazilian
160 Agricultural Research Corporation (EMBRAPA), the US Forest Service, the USAID,
161 and the US Department of State (<http://mapas.cnpm.embrapa.br/paisagens sustentaveis/>).
162 The Asc forest type was represented by 22 plots of 40 m x 40 m each. All the trees with
163 a diameter at breast height (DBH) equal to or greater than 10 cm were measured within
164 each plot. For Fse, 10 sample plots (20 m x 500 m) were used. The field data for the
165 Dense Ombrophilous Forest (Dse) were obtained in 2012 and are described in Silva et
166 al. (2015). The floristic and structural surveys included seven sample plots of 25 m x
167 100 m over mature forests. Trees with DBH equal to or greater than 10 cm were
168 measured within each plot.

169

170 ***2.3. Airborne Laser Scanning (ALS) data***

171 ALS data were acquired by GEOID Ltd. using an Altm 3100/Optech instrument
172 and provided by the Sustainable Landscapes Brazil project. The positional accuracy (1σ)
173 of the LiDAR measurements was approximately 0.10 m horizontally and 0.12 m

174 vertically (<http://mapas.cnpm.embrapa.br/paisagenssustentaveis/>). We focussed our
175 analysis on undisturbed, non-degraded research plots. Structural information was
176 obtained in the Tapajós National Forest, Pará State (September to November 2012), in
177 São Félix do Xingu municipality, Pará state (August 2012) and in Canarana/Querência
178 municipality, Mato Grosso State (August 2012), to represent Dse, Asc and Fse,
179 respectively. Table 1 shows the specifications of LiDAR data for each site.

180 **(Table 1)**

181 ALS data were delivered as classified LAS-formatted point clouds, along with 1-m
182 resolution bare earth digital terrain models (DTM). For comparison with GLAS,
183 discrete-return data were aggregated produce pseudo-waveforms. Coops et al. (2007)
184 demonstrated that canopy profiles, analogue to those derived from full waveform
185 systems, can be derived from discrete return LiDAR when aggregating returns into three
186 dimensional voxel spaces and comparing the amount of discrete returns contained in
187 each voxel layer to the voxel layers below and above. In this study, waveforms were
188 synthesized by sub-setting the LiDAR point cloud co-located with each field plot and
189 counting the number of points observed in vertical bins of 50 cm and at a horizontal
190 resolution of 100 x100m. 10 by 10 pixels of LiDAR metrics were then averaged to
191 match the 1x1km MODIS pixel size. ALS based entropy was then computed to
192 determine canopy structural diversity and approximate canopy roughness (Palace et al.,
193 2015; Stark et al., 2012). The method is described in detail in the next section (2.4) and
194 is analogue to that applied from GLAS observations. In addition to ALS entropy, we
195 also calculated canopy volume models (CVMs) to quantify the three-dimensional
196 structure of the forest canopies based on the incident radiation levels and photosynthetic
197 potential (Coops et al., 2007; Hilker et al., 2010). The method is described in detail in

198 (Lefsky et al., 2005). CVMs divide the canopy space into sunlit and shaded vegetation
199 elements as well as gap spaces enclosed within.

200

201 ***2.4. GLAS/ICESat data and structural metrics from vertical profiles***

202 GLAS profiles were obtained across the Xingu basin (Figure 1) between 2006 and
203 2008 (laser operating periods 3E through 2D) (Gonçalves, 2014). Each GLAS footprint
204 is elliptical in shape, spaced at approximately 170-m intervals along-track. GLAS
205 LiDAR profiles characteristics varied between the campaigns across the study area. The
206 near-infrared elliptical footprint and eccentricity varied between 51.2 (± 1.7) to 58.7
207 (± 0.6), and 0.48 (± 0.02) to 0.59 (± 0.01), respectively. The horizontal and vertical
208 geolocation accuracy varied between 0.00 (± 3.41) to 1.72 (± 7.36), and 0.00 (± 2.38) to
209 1.2 (± 5.14), depending on the campaign and respective data product.

210 Because GLAS observations are able to penetrate optically thin clouds (Schulz et
211 al., 2005), processing of the GLAS profiles included additional cloud screening to
212 improve the data quality. The technique is described in detail in Smith et al. (2005).
213 Briefly, the approach takes advantage of the fact that returns unaffected by saturation or
214 forward scattering resemble narrow Gaussian pulses that are similar to the transmitted
215 pulse (Smith et al., 2005). To process GLAS waveforms, we used parameters reported
216 in the GLA01, GLA05, and GLA14 data products following methods described by
217 (Gonçalves, 2014). First, the waveforms were filtered by convolution with a discrete
218 Gaussian kernel with the same standard deviation as the transmitted laser pulse. This
219 procedure reduced the background noise, while preserving an adequate level of detail
220 for characterization of the canopy (Sun et al., 2008). Second, GLAS waveforms used in
221 this study were calibrated and digitized into 1000 discrete bins at a time resolution of 1
222 ns (~ 15 cm). The locations of the highest (signal start) and lowest (signal end) detected

223 surfaces within the 150-m waveform were determined, respectively, as the first and last
 224 elevations at which the amplitude exceeded a threshold level, for a minimum of n
 225 consecutive bins. The peak of the ground return was determined as the lowest peaks in
 226 the smoothed waveforms with at least the same width as the transmitted laser pulse,
 227 after taking into account the mean noise level. **In order to minimize the effect of**
 228 **different output energy levels of the 2E and 3E Laser flight campaigns, all profiles were**
 229 **then normalized to unity by dividing by the maximum amplitude. This correction**
 230 **approach assumes that differences in measurement campaigns affect the overall amount**
 231 **of energy but do not significantly change the waveforms (i.e. the vertical scale of energy**
 232 **output) of our entropy calculation (Gonçalves, 2014).**

233 We utilized GLAS estimates of entropy (S_z), a measure of canopy structural
 234 diversity sensitive to crown depth and leaf area (Palace et al., 2015; Stark et al., 2012),
 235 as a proxy of canopy roughness. S_z was calculated using Equations 1 and 2 (Harding &
 236 Carabajal, 2005, Nelson et al., 2009, Treuhft et al., 2009, Gonçalves, 2014):

237

$$238 \quad S_z = - \sum_{i=1}^{n_b} p(w_i) \ln(p(w_i)), \quad \text{with} \quad (1)$$

$$240 \quad p(w_i) = \frac{w_i(z)}{\int_0^{H100} w_i(z) dz} \quad (2)$$

242 where n_b is the number of vertical bins from the ground peak to the signal start defined
 243 as the vertical distance between the ground peak and the signal start; $w(z)$ is the laser
 244 power received from the 1m bin centered at height z ; H100 is the maximum canopy

245 height, defined as the vertical distance between the ground peak and the signal start
246 (Gonçalves, 2014).

247

248 *2.5. SeaWinds/QuikSCAT data*

249 Estimates of canopy structure were independently also obtained from SeaWinds
250 Scatterometer data, provided by NASA's Scatterometer Climate Record Pathfinder
251 project. The SeaWinds Scatterometer operates at microwave frequency of 13.4 GHz
252 (Ku-band) with mean incidence angle of 54° for V-polarization and 46° for H-
253 polarization. The sensitivity of radar data to variations in vegetation canopy structure
254 can be explained by the dependence of radar backscatter to surface dielectric properties,
255 which are strongly dependent on the liquid water content of the canopy constituents
256 (Frolking et al., 2006). Given that the SeaWinds instrument operates at a higher
257 frequency and higher incidence angle than other similar sensors, it has lower penetration
258 into forest canopy, and therefore almost no interference from soil moisture variations in
259 densely vegetated forested areas (Saatchi et al., 2013).

260 The backscatter product (σ^0) used in this study combines ascending (morning) and
261 descending (evening) orbital passes, and is based on SeaWinds "egg" images (Frolking
262 et al., 2006). The nominal image pixel resolution for egg images is 4.45 km/pixel. Only
263 backscatter data for horizontal (H) polarization were used, as previous assessments had
264 indicated that results using vertical (V) polarization show no significant differences
265 (Saatchi et al., 2013). We used data obtained from January 2001 to November 2009,
266 when the sensor stopped collecting data due to failure in the scanning capability. To
267 match the spatial resolution of the SeaWinds instrument, we averaged the corresponding
268 anisotropy observations from the MODIS instrument to match the
269 SeaWinds/QuikSCAT pixels.

270 *2.6. Determination of surface anisotropy from multi-angle MODIS data*

271 MODIS observations are acquired at different solar and view zenith angles,
272 depending on the orbital overpass and time of the year. Pixel-based algorithms often
273 assume a Lambertian reflectance model, which reduces the anisotropy of the derived
274 surface reflectance (Lyapustin, 1999; Wang et al., 2010), thus decreasing the ability to
275 detect directional scattering (Hilker et al., 2009). In this study, we use the MAIAC
276 algorithm because it preserves the multi-angle character of MODIS observations,
277 providing a means to estimate the anisotropy of surface reflectance (Chen et al., 2005),
278 a surrogate for structure of vegetation and shaded parts of the canopy (Myneni et al.,
279 2002; Chen et al., 2003; Gao et al., 2003). MAIAC is a cloud screening and atmospheric
280 correction algorithm that uses an adaptive time series analysis and processing of groups
281 of pixels to derive atmospheric aerosol concentration and surface reflectance. A detailed
282 description of the technique can be found in Lyapustin et al. (2011) and Lyapustin et al.
283 (2012). Previous results (Hilker et al., 2012, 2015) have shown that while the MAIAC
284 cloud mask is less conservative, it is also more accurate, improving the number of
285 observations and data quality in tropical environments.

286 For retrieval of the surface bi-directional reflectance distribution function (BRDF),
287 MAIAC accumulates data over 4-16 days (Lyapustin et al., 2011, 2012). Assuming that
288 vegetation is relatively stable during this period, the surface directional scattering can be
289 characterized using the Ross-Thick Li-Sparse (RTLS) bidirectional reflectance
290 distribution function (BRDF) model (Roujean, et al., 1992).

291 Using the RTLS model (Wanner et al., 1995), we characterized the BRDF of each 1
292 km x 1 km grid cell of MODIS data. Based on the RTLS BRDF model, we derived
293 MODIS backscatter (Solar Zenith Angle (SZA) = 45°, View Zenith Angle (VZA) = 35°,
294 Relative Azimuth Angle (RAA) = 180°) and forward scatter (SZA = 45°, VZA = 35°,

295 RAA = 0°) observations (4-16 days of observations) for a fixed view and sun angle. The
296 advantage of using the RTLS model rather than reflectance directly is to keep constant
297 sun-observer geometry and extrapolate measurements to the principal plane. In addition,
298 the modelled reflectance can be based on all multi-angle MODIS data, which should
299 yield a more representative characterization of the reflectance properties. We selected a
300 VZA of 35° rather than the hotspot location at VZA = 45° in order to keep the modelled
301 reflectance closer to the actual range of angles observed by MODIS, thereby
302 minimizing potential errors resulting from extrapolation of the BRDF.

303 We used estimates of anisotropy (defined as the difference between BRDF
304 modelled backscattering (SZA = 45°, VZA = 35°, RAA = 180°) and BRDF modelled
305 forward scattering (SZA = 45°, VZA = 35°, RAA = 0°) based on the Enhanced
306 Vegetation Index (EVI) to describe roughness of the surface for different vegetation
307 types across the study area (Moura et al., 2015). The objective of using EVI rather than
308 surface reflectance of a given band was to minimize the effect of non-photosynthetically
309 active elements (i.e. soil fraction component) while optimizing the sensitivity to green
310 canopy structure (Moura et al., 2015).

311 MODIS-derived anisotropy values were then regressed against ALS-derived
312 entropy, GLAS-derived entropy and SeaWinds/QuikSCAT backscatter (σ^0 , Frolking et
313 al., 2006), which were estimated on a per-pixel-basis to generate time series profiles of
314 entropy for each forest type in the study area.

315

316 **3. Results**

317 The Xingu basin contains a number of different forest types. However, vegetation is
318 dominated by Asc and Dse forest types in the north, and by Fse vegetation in the south,

319 as illustrated in Figure 2. The GLAS tracks are also shown in this figure to highlight the
320 sampling density of the spaceborne LiDAR over each forest type. An illustration of the
321 mean canopy height (MCH) derived from ALS for three sample areas of 1 ha each is
322 provided in Figure 2. Airborne ALS measurements showed, on average, the largest tree
323 heights in the Dse class with values up to 40 meters tall (red color in the inset of Figure
324 2). Asc and Fse vegetation types reached up to 30 m and 25 meters in height,
325 respectively. Field measurements showed that mean canopy heights from forest
326 inventories were 19.8 m, 17.4 m and 17.0 m for Dse, Asc and Fse, respectively (Table
327 2). When compared to Asc and Fse, Dse presented larger metrics of diversity (i.e.
328 species richness (S) and Shannon index (H')) and structure (mean height (H_T), mean
329 diameter at breast height (DBH), basal area (BA), aboveground biomass (AGB) and leaf
330 area index (LAI)) (Table 2).

331

332 **(Figure 2)**

333

334 **(Table 2)**

335 Differences in canopy structure were also evident from the analysis of canopy
336 volume models (CVMs) (Figure 3). While gap spaces were relatively small in all three
337 vegetation types, Asc showed a notably higher proportion of sunlit vegetation that
338 reached down deep into the canopy, suggesting a higher spatial variability of tree
339 heights compared to the other two vegetation types. Similarly, gaps in the upper canopy
340 were mostly present in Asc, as expected for open forest types. Fse showed gaps
341 predominantly in lower height levels, and a higher overall proportion of shaded crown.
342 Full canopy closure (100% of the canopy space filled by either sunlit or shaded canopy

343 elements or fully enclosed gap space) was reached at about 15 m height for both Asc
344 and Dse, and at about 20 m height for Fse.

345 **(Figure 3)**

346

347 Differences in vegetation structure derived from ALS data were confirmed also
348 with spaceborne GLAS observations. GLAS-derived seasonal profiles of entropy for
349 2006 showed spatial averages that differed over time between the three vegetation types
350 (Figure 4). Even though there were differences in the years of data acquisition (2006 for
351 GLAS and 2012 for ALS), the shaded area in Figure 4 was plotted to provide a seasonal
352 reference between the airborne and spaceborne data. GLAS derived seasonal profiles
353 varied between different forest types. The lowest values of entropy were consistently
354 found for Fse. In contrast, Asc for Dse showed GLAS entropy higher throughout the
355 measurement period. All forest types showed strong seasonality with increasing entropy
356 from February to September, and decreasing values thereafter with predominance of
357 higher entropy during the dry season.

358

359 **(Figure 4)**

360 Examples of MODIS anisotropy during March, June and October of 2006
361 illustrated seasonal and spatial changes in multi-angle reflectance across the Xingu
362 basin (Figure 5). The MODIS derived anisotropy was consistently higher in the northern
363 part of the study area, and its spatial distribution coincided well with the forest types
364 indicated in Figure 2. A clear limit between forested (high MODIS anisotropy) and non-
365 forested (low anisotropy) areas was evident in the southern part of the map.
366 Furthermore, higher values of anisotropy were found for the Asc and Dse vegetation
367 compared to Fse. While MAIAC observations allowed a notable number of

368 measurements of anisotropy between June (Figure 5b) and October (Figure 5c), some
369 data gaps were observed in March (Figure 5a) due to cloud cover in the rainy season.

370 **(Figure 5)**

371 MODIS-derived anisotropy was linearly correlated to ALS-derived entropy
372 (Figure 6). The coefficient of determination (r^2) of the relationship between all 828
373 MODIS pixels that coincided with existing ALS observations was 0.54 with an RMSE
374 of 0.11 units of entropy. Much of the scattering presented in Figure 3 was limited to
375 lower values of entropy, while residuals were notably smaller for the higher entropy
376 range.

377 **(Figure 6)**

378 Significant relationships were also found between MODIS anisotropy and
379 GLAS measured entropy using all observations that contained five or more GLAS shots
380 within the 1 km x 1 km MODIS pixels (Figure 7). In order to examine seasonal
381 variability in the relationship, we performed the regressions separately for March
382 (Figure 7a), June (Figure 7b) and October (Figure 7c) of 2006. The r^2 varied between
383 0.52 for March and 0.61 for June ($p < 0.05$) with similar slopes and offsets found
384 throughout the observation period. RMSE varied between 0.26 and 0.30 units of entropy.
385 The highest noise levels were observed in March, which is corresponding also to the
386 larger amount of data gaps during the rainy season (Figure 5). The availability of GLAS
387 data was somewhat limited during June, but the relationships were still highly
388 significant and consistent with those observed during other months of the year. A
389 comparison between conventional VI estimates using directionally normalized EVI
390 from MAIAC and LiDAR derived Entropy is shown in the appendix (Figure A1).

391 **(Figure 7)**

392 A strong relationship between the MODIS-derived anisotropy and the
393 backscattering measurements (σ^0) from SeaWinds/QuikSCAT was also observed
394 (Figure 8). The relationship was obtained for 10.000 randomly sampled MODIS pixels
395 and corresponding SeaWinds/QuikSCAT (σ^0) observations across the Xingu basin for
396 all available QuikSCAT data between 2001 and 2009. Note, however, that when using
397 radar observations, the relationship to MODIS-derived anisotropy was non-linear
398 ($r^2=0.59$, RMSE=0.11).

399 (Figure 8)

400 Time series profiles of MODIS-derived entropy estimated from the regression
401 model of Figure 7c and of MODIS-derived QuikSCAT- σ^0 estimated from model of
402 Figure 8 were plotted as spatial averages for Dse, Asc and Fse (Figure 9). All three
403 forest types displayed notable seasonal cycles. The Ombrophilous Forests (Dse and Asc)
404 consistently showed high values of entropy with less seasonal variation. In contrast, the
405 seasonal cycles were much more pronounced in the Fse, as expected for semi-deciduous
406 vegetation. Both models (GLAS-derived entropy and QScat-derived σ^0) yielded very
407 similar seasonal patterns, in terms of temporal variation as well as in terms of
408 differences between vegetation types. The results presented in Figure 9 were consistent
409 also with those shown in Figure 5. A small negative trend in both entropy and σ^0 was
410 observed from 2000 until 2009 and a positive trend in all three vegetation types was
411 found from 2010 onwards. This trend was especially pronounced for the canopy entropy
412 based on GLAS observations.

413 (Figure 9)

414 4. Discussion

415 This study investigated the potential of multi-angle reflectance obtained from
416 MODIS to derive estimates of vegetated surface roughness as an important structural

417 parameter of land atmosphere interactions. Aside from field observations, airborne laser
418 scanning is arguably the most comprehensive tool to describe the three-dimensional
419 vegetation structure at the stand level to date (Coops et al., 2007; Lim et al., 2003;
420 Wulder et al., 2012). Recent initiatives such as the “Sustainable Landscapes
421 Brazil” project (<http://mapas.cnpm.embrapa.br/paisagenssustentaveis/>) seek to improve
422 upon existing deficiencies of data availability and provide new opportunities to generate
423 structural metrics across discrete locations within the Amazon basin.

424 LiDAR based characterization of vegetation structure (Figures 2, 3, and Table 1)
425 exposed a large heterogeneity across the Xingu basin, both spatially and seasonally.
426 ALS-observed structural differences between vegetation types were detectable also
427 from space using photon counting LiDAR (GLAS/IceSat) and microwave
428 backscattering (SeaWinds/QuikSCAT) (Figures 4 and 9b). This is an important finding,
429 as it opens an opportunity for scaling spatially discrete observations of canopy structure
430 across larger areas from space (Popescu et al., 2011).

431 Spatial and temporal heterogeneity in Amazonian vegetation (Silva et al., 2013;
432 Townsend et al., 2008) is not easily obtained from conventional vegetation indices
433 (Hilker et al., 2015), as VIs cannot adequately capture differences in canopy structure
434 among different vegetation types (Glenn et al., 2008; Lagouarde et al., 2002). Findings
435 presented in this study (Figures 6 to 9) suggest that such canopy structural variation may
436 be better determined from multi-angular reflectance. Our estimates of anisotropy
437 showed considerable improvements over estimates using mono-observation vegetation
438 indices (Figure A1). The ability of multi-angle observation to derive vegetation
439 structural attributes is well supported by previous results (Chen & Leblanc, 1997; Chen,
440 2003; Gao, 2003; Strahler & Jupp, 1990; Yu et al., 2015; Zhang et al., 2002). While
441 these authors have focused on smaller study areas using specialized sensors, our

442 findings confirm such multi-angle potential to be acquired from the MODIS instrument
443 and across the Amazon basin (Moura et al., 2015). Our previous work also confirmed
444 the consistency of monthly anisotropy measurements and its statistical significance for
445 estimating seasonal changes in vegetation structure across the Amazon (Moura et al.,
446 2015). This is an important advancement, as it allows structural estimates over large
447 areas and at high temporal frequencies from space, complementing the data analysis of
448 orbital LiDAR data.

449 Anisotropy derived from multiple overpasses of MODIS imagery may therefore
450 provide new insights into structural variability of Amazon forests as it increases the
451 sensitivity to changes in vegetation structure across dense vegetation types. As
452 demonstrated in previous work (Moura et al., 2015), seasonal changes in observed
453 anisotropy cannot be explained by bi-directional effects, as all observations have been
454 normalized to a fixed forward and backscatter geometry (Lyapustin et al., 2012b). In
455 addition, Moura et al. (2015) demonstrated that standard deviations between observed
456 and modelled MAIAC reflectance were about 10% of the observed variation in
457 anisotropy, thus confirming the ability of our approach to detect seasonal and inter-
458 annual changes. Differences between forward and backscatter observations as utilized in
459 this paper are largely driven by the different directional scattering behaviour of red and
460 NIR reflectance (Moura et al., 2015, Hilker et al., 2015). The modelled near hotspot and
461 near darkspot locations were designed to maximize the range of resulting anisotropy,
462 thereby seeking to increase the sensitivity with respect to changes in vegetation
463 structure.

464 While the range of view angles acquired by MODIS is relatively small, as the
465 instrument was not specifically designed for multi-angle acquisitions, MODIS-derived
466 anisotropy still provided an effective means to characterize vegetation structure across

467 large areas from space. Within the Amazon basin (or tropics in general), this is partially
468 facilitated by the fact that MODIS view geometry comes very close to the principal
469 plane twice a year. As a result, our BRDF model is representative of the angles used in
470 this study. Consequently, modelled anisotropy is close to its maximum range of possible
471 values. The contrary occurs in mid-latitudes where observations are further from the
472 principal plane. In these cases, other geometric configurations might be preferable.

473 Modelling MODIS anisotropy using the RTLS BRDF model further allowed us to
474 derive anisotropy independent of the sun-observer geometry (Roujean et al., 1992). As a
475 limitation to this approach, changes in sun-sensor configuration over the year do not
476 always allow modelling of forward and backscattering observations within the sampling
477 range of the MODIS instruments. Therefore, higher uncertainties may be observed
478 during some times of the year than during others.

479 The strong, positive correlation found between GLAS-measured entropy and
480 MODIS anisotropy (Figure 6) may be explained by geometric scattering of individual
481 tree crowns (Chopping et al., 2011; Li, X., Strahler, 1986). For instance, a large
482 variability in canopy heights (high canopy roughness) will increase the geometric
483 scattering component, especially of NIR reflectance. Other structural changes may,
484 however, also influence seasonal patterns of anisotropy. In addition to canopy
485 roughness, anisotropy is also affected by leaf angle distribution (Roujean, 2002) and
486 foliage clumping (Chen et al., 2005) among other variables related to the floristic
487 variability, which tends to be high in tropical forests. The interaction between these
488 variables and multi-angle scattering is not straightforward, requiring further
489 investigation, especially in the components of scattering determined in the RTLS model.
490 For example, increases in leaf area may increase the volumetric scattering component
491 (Ross, 1981; Roujean, et al., 1992) of multi-angle reflectance, but at the same time

492 decrease the surface roughness, at least within a certain range of values. Therefore, the
493 results presented in here should be understood as a first demonstration of the technique.

494 Due to the complexities described as well as other limitations in terms of footprint
495 size, and range of angular sampling, MODIS-derived estimates of canopy structure
496 should not be understood as a replacement for direct 3D measures of vegetation, but
497 rather as a complimentary approach for scaling such observations in space and time.
498 The consistency in the modelled relationship obtained from GLAS LiDAR and
499 SeaWinds/QuikSCAT backscattering is encouraging in this respect, as it suggests that
500 such scaling approaches may be built on opportunistically sampled observations across
501 platforms. For instance, MODIS data can help interpret estimates of canopy roughness
502 in between GLAS footprints, as well as fill missing observations in time, enabling more
503 comprehensive seasonal and spatial analysis. Upcoming new LiDAR instruments, such
504 as the Global Ecosystem Dynamics (GEDI) mission (Dubayah et al., 2014; Stysley et al.,
505 2015), will allow further improvements in the measures of canopy structure as well as
506 biomass.

507

508 **5. Conclusions**

509 Our analysis has demonstrated that multi-angular MODIS observations are suitable
510 to determine canopy entropy at different scales of LiDAR measurements across the
511 study area in the Amazon. The sparseness of existing, highly detailed LiDAR
512 observations currently imposes severe restriction on accuracy of modeled carbon and
513 water fluxes, particularly in remote regions such as the Amazon basin. Complementary
514 measures of vegetation structure from optical satellites are therefore highly desirable to
515 extrapolate spatially or temporally sparse estimates of canopy structure across the

516 landscape. Such approaches will be crucial for improving our understanding of climate
517 tolerance and responses to Amazonian forests to extreme events.

518

519 **Acknowledgements**

520 We are grateful to the NASA Center for Climate Simulation (NCCS) for
521 computational support and access to their high performance cluster. MAIAC data for
522 the amazon basin are described and available for download at
523 <ftp://ladsweb.nascom.nasa.gov/MAIAC>. LiDAR data were acquired by the Sustainable
524 Landscapes Brazil project supported by the Brazilian Agricultural Research Corporation
525 (EMBRAPA), the US Forest Service, and USAID, and the US Department of State.
526 Thanks are also to CAPES (Coordenação de Aperfeiçoamento de Pessoal de Nível
527 Superior) grant number 12881-13-9; and CNPq (Conselho Nacional de
528 Desenvolvimento Científico e Tecnológico), grant number PVE 401025/2014-4. Dr
529 Eduardo Maeda was supported by a research grant from the Academy of Finland.

530

531 **References**

- 532 Asner, G. P., & Alencar, A. (2010). Drought impacts on the Amazon forest: the remote
533 sensing perspective. *The New Phytologist*, 187(3), 569–78. doi:10.1111/j.1469-
534 8137.2010.03310.x
- 535 Barnsley, M. J., Settle, J. J., Cutter, M. A., Lobb, D. R., & Teston, F. (2004). The
536 PROBA/CHRIS mission: a low-cost smallsat for hyperspectral multiangle
537 observations of the Earth surface and atmosphere. *IEEE Transactions on*
538 *Geoscience and Remote Sensing*, 42(7), 1512–1520.
539 doi:10.1109/TGRS.2004.827260
- 540 BOUDREAU, J., NELSON, R., MARGOLIS, H., BEAUDOIN, A., GUINDON, L., &
541 KIMES, D. (2008). Regional aboveground forest biomass using airborne and
542 spaceborne LiDAR in Québec. *Remote Sensing of Environment*, 112(10), 3876–
543 3890. doi:10.1016/j.rse.2008.06.003
- 544 Breunig, F. M., Galvão, L. S., dos Santos, J. R., Gitelson, A. A., de Moura, Y. M., Teles,
545 T. S., & Gaida, W. (2015). Spectral anisotropy of subtropical deciduous forest
546 using MISR and MODIS data acquired under large seasonal variation in solar
547 zenith angle. *International Journal of Applied Earth Observation and*

- 548 *Geoinformation*, 35, 294–304. doi:10.1016/j.jag.2014.09.017
- 549 Carlson, T. N., & Ripley, D. A. (1997). On the relation between NDVI, fractional
550 vegetation cover, and leaf area index. *Remote Sensing of Environment*, 62(3), 241–
551 252. doi:10.1016/S0034-4257(97)00104-1
- 552 Chapin, F. I., Matson, P., & Vitousek, P. (2011). *Principles of terrestrial ecosystem*
553 *ecology*. Retrieved from
554 [https://books.google.com/books?hl=en&lr=&id=68nFNpceRmIC&oi=fnd&pg=PR](https://books.google.com/books?hl=en&lr=&id=68nFNpceRmIC&oi=fnd&pg=PR5&dq=principles+of+terrestrial+ecosystem+ecology+stuart&ots=V1DZdx8sni&sig=d5RF0D75OjOWRvQpqdU9k1hxqkI)
555 [5&dq=principles+of+terrestrial+ecosystem+ecology+stuart&ots=V1DZdx8sni&si](https://books.google.com/books?hl=en&lr=&id=68nFNpceRmIC&oi=fnd&pg=PR5&dq=principles+of+terrestrial+ecosystem+ecology+stuart&ots=V1DZdx8sni&sig=d5RF0D75OjOWRvQpqdU9k1hxqkI)
556 [g=d5RF0D75OjOWRvQpqdU9k1hxqkI](https://books.google.com/books?hl=en&lr=&id=68nFNpceRmIC&oi=fnd&pg=PR5&dq=principles+of+terrestrial+ecosystem+ecology+stuart&ots=V1DZdx8sni&sig=d5RF0D75OjOWRvQpqdU9k1hxqkI)
- 557 Chen, J. M., & Leblanc, S. G. (1997). A four-scale bidirectional reflectance model
558 based on canopy architecture. *IEEE Transactions on Geoscience and Remote*
559 *Sensing*, 35(5), 1316–1337. doi:10.1109/36.628798
- 560 Chen, J. M., Liub, J., Leblanc, S. G., Lacazec, R., & Roujean, J. L. (2003). Multi-
561 angular optical remote sensing for assessing vegetation structure and carbon
562 absorption.
- 563 Chen, J. M., Menges, C. H., & Leblanc, S. G. (2005). Global mapping of foliage
564 clumping index using multi-angular satellite data. *Remote Sensing of Environment*,
565 97(4), 447–457. doi:10.1016/j.rse.2005.05.003
- 566 Chopping, M., Schaaf, C. B., Zhao, F., Wang, Z., Nolin, A. W., Moisen, G. G.,
567 Martonchik, J. V., & Bull, M. (2011). Forest structure and aboveground biomass in
568 the southwestern United States from MODIS and MISR. *Remote Sensing of*
569 *Environment*, 115(11), 2943–2953. doi:10.1016/j.rse.2010.08.031
- 570 Coops, N. C., Hilker, T., Wulder, M. A., St-Onge, B., Newnham, G., Siggins, A., &
571 Trofymow, J. A. (Tony). (2007). Estimating canopy structure of Douglas-fir forest
572 stands from discrete-return LiDAR. *Trees*, 21(3), 295–310. doi:10.1007/s00468-
573 006-0119-6
- 574 Domingues, T. F., Berry, J. A., Martinelli, L. A., Ometto, J. P. H. B., & Ehleringer, J. R.
575 (2005). Parameterization of Canopy Structure and Leaf-Level Gas Exchange for an
576 Eastern Amazonian Tropical Rain Forest (Tapajós National Forest, Pará, Brazil).
577 *Earth Interactions*, 9(17), 1–23. doi:10.1175/EI149.1
- 578 Dubayah, R., Goetz, S. J., Blair, J. B., Fatoyinbo, T. E., Hansen, M., Healey, S. P.,
579 Hofton, M. A., Hurtt, G. C., Kellner, J., Luthcke, S. B., & Swatantran, A.
580 (2014). The Global Ecosystem Dynamics Investigation. *American Geophysical*
581 *Union*. Retrieved from <http://adsabs.harvard.edu/abs/2014AGUFM.U14A..07D>
- 582 Frolking, S., Milliman, T., McDonald, K., Kimball, J., Zhao, M., & Fahnestock, M.
583 (2006). Evaluation of the Sea Winds scatterometer for regional monitoring of
584 vegetation phenology. *Journal of Geophysical Research: Atmospheres*, 111(17), 1–
585 14. doi:10.1029/2005JD006588
- 586 Frolking, S., Milliman, T., Palace, M., Wisser, D., Lammers, R., & Fahnestock, M.
587 (2011). Tropical forest backscatter anomaly evident in SeaWinds scatterometer
588 morning overpass data during 2005 drought in Amazonia. *Remote Sensing of*
589 *Environment*, 115(3), 897–907. doi:10.1016/j.rse.2010.11.017
- 590 Gao, F. (2003). Detecting vegetation structure using a kernel-based BRDF model.
591 *Remote Sensing of Environment*, 86(2), 198–205. doi:10.1016/S0034-
592 4257(03)00100-7
- 593 Glenn, E. P., Huete, A. R., Nagler, P. L., & Nelson, S. G. (2008). Relationship between

- 594 remotely-sensed vegetation indices, canopy attributes and plant physiological
595 processes: What vegetation indices can and cannot tell us about the landscape.
596 *Sensors*, 8(4), 2136–2160. doi:10.3390/s8042136
- 597 Gonçalves, F. G. (2016, January). Vertical structure and aboveground biomass of
598 tropical forests from lidar remote sensing.
- 599 Harding, D. J. (2005). ICESat waveform measurements of within-footprint topographic
600 relief and vegetation vertical structure. *Geophysical Research Letters*, 32(21),
601 L21S10. doi:10.1029/2005GL023471
- 602 Hilker, T., Leeuwen, M., Coops, N. C., Wulder, M. A., Newnham, G. J., Jupp, D. L. B.,
603 & Culvenor, D. S. (2010). Comparing canopy metrics derived from terrestrial and
604 airborne laser scanning in a Douglas-fir dominated forest stand. *Trees*, 24(5), 819–
605 832. doi:10.1007/s00468-010-0452-7
- 606 Hilker, T., Lyapustin, A. I., Hall, F. G., Myneni, R., Knyazikhin, Y., Wang, Y., Tucker,
607 C. J., & Sellers, P. J. (2015). On the measurability of change in Amazon vegetation
608 from MODIS. *Remote Sensing of Environment*, 166, 233–242.
609 doi:10.1016/j.rse.2015.05.020
- 610 Hilker, T., Wulder, M. A., Coops, N. C., Linke, J., McDermid, G., Masek, J. G., Gao, F.,
611 & White, J. C. (2009). A new data fusion model for high spatial- and temporal-
612 resolution mapping of forest disturbance based on Landsat and MODIS. *Remote
613 Sensing of Environment*, 113(8), 1613–1627. doi:10.1016/j.rse.2009.03.007
- 614 IBGE. (2004). *Manual Técnico da vegetação brasileira*.
- 615 Jing M. Chena, Jane Liub, Sylvain G. Leblancb, Roselyne Lacazec, J.-L. R. (2002).
616 Multi-angular optical remote sensing for assessing vegetation structure and carbon
617 absorption. *Remote Sensing of Environment*, 84, 516–525.
- 618 Lagouarde, J.-P., Jacob, F., Gu, X. F., Olioso, A., Bonnefond, J.-M., Kerr, Y., John
619 Mcaneney, K., & Irvine, M. (2002). Spatialization of sensible heat flux over a
620 heterogeneous landscape. *Agronomie*, 22(6), 627–633. doi:10.1051/agro:2002032
- 621 Lefsky, M. A., Harding, D. J., Keller, M., Cohen, W. B., Carabajal, C. C., Del Bom
622 Espirito-Santo, F., Hunter, M. O., & de Oliveira, R. (2005). Estimates of forest
623 canopy height and aboveground biomass using ICESat. *Geophysical Research
624 Letters*, 32(22), L22S02. doi:10.1029/2005GL023971
- 625 Li, X., Strahler, A. H. (1986). Geometric-Optical Bidirectional Reflectance Modeling of
626 a Conifer Forest Canopy, (6), 906–919.
- 627 Lim, K., Treitz, P., Wulder, M., St-Onge, B., & Flood, M. (2003). LiDAR remote
628 sensing of forest structure. *Progress in Physical Geography*, 27(1), 88–106.
629 doi:10.1191/0309133303pp360ra
- 630 LYAPUSTIN, A. I., & MULDASHEV, T. Z. (1999). METHOD OF SPHERICAL
631 HARMONICS IN THE RADIATIVE TRANSFER PROBLEM WITH NON-
632 LAMBERTIAN SURFACE. *Journal of Quantitative Spectroscopy and Radiative
633 Transfer*, 61(4), 545–555. doi:10.1016/S0022-4073(98)00041-7
- 634 Lyapustin, A. I., Wang, Y., Laszlo, I., Hilker, T., G.Hall, F., Sellers, P. J., Tucker, C. J.,
635 & Korkin, S. V. (2012a). Multi-Angle Implementation of Atmospheric Correction
636 for MODIS (MAIAC). Part 3: Atmospheric Correction. *Remote Sensing of
637 Environment*, 127, 385–393. doi:10.1016/j.rse.2012.09.002
- 638 Lyapustin, A., Wang, Y., Laszlo, I., & Hilker, T. (2012b). Multi-Angle Implementation

- 639 of Atmospheric Correction for MODIS (MAIAC). Part 3: Atmospheric Correction.
 640 *Remote Sensing of Environment*, 127, 385–393. Retrieved from
 641 <http://ntrs.nasa.gov/search.jsp?R=20120017006>
- 642 Moura, Y. M. de, Hilker, T., Lyapustin, A. I., Galvão, L. S., dos Santos, J. R., Anderson,
 643 L. O., de Sousa, C. H. R., & Arai, E. (2015). Seasonality and drought effects of
 644 Amazonian forests observed from multi-angle satellite data. *Remote Sensing of*
 645 *Environment*, 171, 278–290. doi:10.1016/j.rse.2015.10.015
- 646 Moura, Y. M., Galvão, L. S., dos Santos, J. R., Roberts, D. a., & Breunig, F. M. (2012).
 647 Use of MISR/Terra data to study intra- and inter-annual EVI variations in the dry
 648 season of tropical forest. *Remote Sensing of Environment*, 127, 260–270.
 649 doi:10.1016/j.rse.2012.09.013
- 650 Myneni, R. ., Hoffman, S., Knyazikhin, Y., Privette, J. ., Glassy, J., Tian, Y., Wang, Y.,
 651 Song, X., Zhang, Y., Smith, G. ., Lotsch, A., Friedl, M., Morisette, J. ., Votava, P.,
 652 Nemani, R. ., & Running, S. . (2002). Global products of vegetation leaf area and
 653 fraction absorbed PAR from year one of MODIS data. *Remote Sensing of*
 654 *Environment*, 83(1-2), 214–231. doi:10.1016/S0034-4257(02)00074-3
- 655 Myneni, R. B., Yang, W., Nemani, R. R., Huete, A. R., Dickinson, R. E., Knyazikhin,
 656 Y., Didan, K., Fu, R., Negrón Juárez, R. I., Saatchi, S. S., Hashimoto, H., Ichii, K.,
 657 Shabanov, N. V., Tan, B., Ratana, P., Privette, J. L., Morisette, J. T., ...
 658 Salomonson, V. V. (2007). Large seasonal swings in leaf area of Amazon
 659 rainforests. *Proceedings of the National Academy of Sciences of the United States*
 660 *of America*, 104(12), 4820–3. doi:10.1073/pnas.0611338104
- 661 Palace, M. W., Sullivan, F. B., Ducey, M. J., Treuhaft, R. N., Herrick, C., Shimbo, J. Z.,
 662 & Mota-E-Silva, J. (2015). Estimating forest structure in a tropical forest using
 663 field measurements, a synthetic model and discrete return lidar data. *Remote*
 664 *Sensing of Environment*, 161, 1–11. doi:10.1016/j.rse.2015.01.020
- 665 Pang, Y., Lefsky, M., Sun, G., Miller, M. E., & Li, Z. (2008). Temperate forest height
 666 estimation performance using ICESat GLAS data from different observation
 667 periods, 37.
- 668 Popescu, S. C., Zhao, K., Neuenschwander, A., & Lin, C. (2011). Satellite lidar vs.
 669 small footprint airborne lidar: Comparing the accuracy of aboveground biomass
 670 estimates and forest structure metrics at footprint level. *Remote Sensing of*
 671 *Environment*, 115(11), 2786–2797. doi:10.1016/j.rse.2011.01.026
- 672 Ross, I. (1981). *The radiation regime and architecture of plant stands*.
- 673 Roujean, J. J.-L., Leroy, M., & Deschamps, P.-Y. (1992). A bidirectional reflectance
 674 model of the Earth's surface for the correction of remote sensing data. *Journal of*
 675 *Geophysical Research*, 97(D18), 20455–20468. doi:10.1029/92JD01411
- 676 Roujean, J.-L. (2002). Global mapping of vegetation parameters from POLDER
 677 multiangular measurements for studies of surface-atmosphere interactions: A
 678 pragmatic method and its validation. *Journal of Geophysical Research*, 107(D12),
 679 4150. doi:10.1029/2001JD000751
- 680 Saatchi, S., Asefi-Najafabady, S., Malhi, Y., Aragão, L. E. O. C., Anderson, L. O.,
 681 Myneni, R. B., & Nemani, R. (2013). Persistent effects of a severe drought on
 682 Amazonian forest canopy. *Proceedings of the National Academy of Sciences of the*
 683 *United States of America*, 110(2), 565–70. doi:10.1073/pnas.1204651110
- 684 Schutz, B. E., Zwally, H. J., Shuman, C. A., Hancock, D., & DiMarzio, J. P. (2005).

- 685 Overview of the ICESat Mission. *Geophysical Research Letters*, 32(21), L21S01.
686 doi:10.1029/2005GL024009
- 687 Shaw, R. H., & Pereira, A. . (1982). Aerodynamic roughness of a plant canopy: A
688 numerical experiment. *Agricultural Meteorology*, 26(1), 51–65. doi:10.1016/0002-
689 1571(82)90057-7
- 690 Silva, F. B., Shimabukuro, Y. E., Aragão, L. E. O. C., Anderson, L. O., Pereira, G.,
691 Cardozo, F., & Arai, E. (2013). Large-scale heterogeneity of Amazonian
692 phenology revealed from 26-year long AVHRR/NDVI time-series. *Environmental*
693 *Research Letters*, 8(2), 024011. doi:10.1088/1748-9326/8/2/024011
- 694 Stark, S. C., Leitold, V., Wu, J. L., Hunter, M. O., de Castilho, C. V, Costa, F. R. C.,
695 McMahon, S. M., Parker, G. G., Shimabukuro, M. T., Lefsky, M. A., Keller, M.,
696 Alves, L. F., Schiatti, J., Shimabukuro, Y. E., Brandão, D. O., Woodcock, T. K.,
697 Higuchi, N., ... Chave, J. (2012). Amazon forest carbon dynamics predicted by
698 profiles of canopy leaf area and light environment. *Ecology Letters*, 15(12), 1406–
699 14. doi:10.1111/j.1461-0248.2012.01864.x
- 700 Strahler, A. H. (2009). Vegetation canopy reflectance modeling—recent developments
701 and remote sensing perspectives* . *Remote Sensing Reviews*, 15(1-4), 179–194.
702 doi:10.1080/02757259709532337
- 703 Strahler, A. H., Jupp, D. L. ., Woodcock, C. E., Schaaf, C. B., Yao, T., Zhao, F., Yang,
704 X., Lovell, J., Culvenor, D., Newnham, G., Ni-Miester, W., & Boykin-Morris, W.
705 (2008). Retrieval of forest structural parameters using a ground-based lidar
706 instrument (Echidna ®). *Canadian Journal of Remote Sensing*, 34(S2), S426–
707 S440. doi:10.5589/m08-046
- 708 Strahler, A. H., & Jupp, D. L. B. (1990). Modeling bidirectional reflectance of forests
709 and woodlands using boolean models and geometric optics. *Remote Sensing of*
710 *Environment*, 34(3), 153–166. doi:10.1016/0034-4257(90)90065-T
- 711 Stysley, P. R., Coyle, D. B., Kay, R. B., Frederickson, R., Poullos, D., Cory, K., &
712 Clarke, G. (2015). Long term performance of the High Output Maximum
713 Efficiency Resonator (HOMER) laser for NASA's Global Ecosystem Dynamics
714 Investigation (GEDI) lidar. *Optics & Laser Technology*, 68, 67–72.
715 doi:10.1016/j.optlastec.2014.11.001
- 716 SUN, G., RANSON, K., KIMES, D., BLAIR, J., & KOVACS, K. (2008). Forest
717 vertical structure from GLAS: An evaluation using LVIS and SRTM data. *Remote*
718 *Sensing of Environment*, 112(1), 107–117. doi:10.1016/j.rse.2006.09.036
- 719 Townsend, A. R., Asner, G. P., & Cleveland, C. C. (2008). The biogeochemical
720 heterogeneity of tropical forests. *Trends in Ecology & Evolution*, 23(8), 424–31.
721 doi:10.1016/j.tree.2008.04.009
- 722 Vieira, S., de Camargo, P. B., Selhorst, D., da Silva, R., Hutyra, L., Chambers, J. Q.,
723 Brown, I. F., Higuchi, N., dos Santos, J., Wofsy, S. C., Trumbore, S. E., &
724 Martinelli, L. A. (2004). Forest structure and carbon dynamics in Amazonian
725 tropical rain forests. *Oecologia*, 140(3), 468–79. doi:10.1007/s00442-004-1598-z
- 726 Vourlitis, G. L., de Souza Nogueira, J., de Almeida Lobo, F., & Pinto, O. B. (2015).
727 Variations in evapotranspiration and climate for an Amazonian semi-deciduous
728 forest over seasonal, annual, and El Niño cycles. *International Journal of*
729 *Biometeorology*, 59(2), 217–30. doi:10.1007/s00484-014-0837-1
- 730 Walthall, C. L. (1997). A Study of Reflectance Anisotropy and Canopy Structure Using

- 731 a Simple Empirical Model. *Remote Sensing of Environment*, 128(May 1995), 118–
732 128.
- 733 Wang, Y., Lyapustin, A. I. A., Privette, J. J. L., Cook, R. B., SanthanaVannan, S. K.,
734 Vermote, E. F., & Schaaf, C. L. (2010). Assessment of biases in MODIS surface
735 reflectance due to Lambertian approximation. *Remote Sensing of ...*, 114(11),
736 2791–2801. doi:10.1016/j.rse.2010.06.013
- 737 Wanner, W., Li, X., & Strahler, A. H. (1995). On the derivation of kernels for kernel-
738 driven models of bidirectional reflectance. *Journal of Geophysical Research*,
739 100(D10), 21077. doi:10.1029/95JD02371
- 740 WIDLÓWSKI, J.-L., PINTY, B., GOBRON, N., Verstraete, M. M., Diner, D. J., &
741 Davis, A. B. (2004). Canopy Structure Parameters Derived from Multi-Angular
742 Remote Sensing Data for Terrestrial Carbon Studies. *Climatic Change*, 67(2-3),
743 403–415. doi:10.1007/s10584-004-3566-3
- 744 Widłowski, J.-L., Pinty, B., Lavergne, T., Verstraete, M. M., & Gobron, N. (2005).
745 Using 1-D models to interpret the reflectance anisotropy of 3-D canopy targets:
746 issues and caveats. *IEEE Transactions on Geoscience and Remote Sensing*, 43(9),
747 2008–2017. doi:10.1109/TGRS.2005.853718
- 748 Wulder, M. a., White, J. C., Nelson, R. F., Næsset, E., Ørka, H. O., Coops, N. C., Hilker,
749 T., Bater, C. W., & Gobakken, T. (2012). Lidar sampling for large-area forest
750 characterization: A review. *Remote Sensing of Environment*, 121, 196–209.
751 doi:10.1016/j.rse.2012.02.001
- 752 Yu, Y., Yang, X., & Fan, W. (2015). Estimates of forest structure parameters from
753 GLAS data and multi-angle imaging spectrometer data. *International Journal of*
754 *Applied Earth Observation and Geoinformation*, 38, 65–71.
755 doi:10.1016/j.jag.2014.12.013
- 756 Zhang, Y., Tian, Y., Myneni, R. B., Knyazikhin, Y., & Woodcock, C. E. (2002).
757 Assessing the information content of multiangle satellite data for mapping biomes.
758 *Remote Sensing of Environment*, 80(3), 418–434. Retrieved from
759 <http://www.sciencedirect.com/science/article/pii/S0034425701003224>
- 760 Zwally, H. J., Schutz, B., Abdalati, W., Abshire, J., Bentley, C., Brenner, A., Bufton, J.,
761 Dezio, J., Hancock, D., Harding, D., Herring, T., Minster, B., Quinn, K., Palm, S.,
762 Spinhirne, J., & Thomas, R. (2002). ICESat's laser measurements of polar ice,
763 atmosphere, ocean, and land. *Journal of Geodynamics*, 34(3-4), 405–445.
764 doi:10.1016/S0264-3707(02)00042-X
- 765
- 766
- 767
- 768
- 769
- 770

LIST OF TABLES

771

772

773 Table 1. Characteristics of the airborne laser scanning (ALS) data acquired over Dense
774 Ombrophilous (Dse), Open Ombrophilous (Asc) and Semi-Deciduous (Fse) Forests in
775 the Brazilian Amazon.

776

Forest Type	Total area (ha)	Max flight altitude (m)	Flightline overlap (%)	Average return density (ppm ²)	Average first return density (ppm ²)	Field of view (°)
Dse	1049	850	65	25.1	15.28	11.1
Asc	1004	850	65	24.1	15.20	11.0
Fse	1005	850	65	13.7	7.05	11.0

777

778

779 Table 2. Floristic and structural metrics calculated from field inventory data for Dense
780 Ombrophilous Forest (Dse), Open Ombrophilous Forest (Asc) and Semi-Deciduous
781 Forest (Fse). The mean leaf area index (LAI), determined from Airborne Laser
782 Scanning (ALS), is indicated in the last column of the table.

Forest Type	Plots	S	H'	Ht(m)	BA _(m² m⁻²)	LAI _(ALS)
Dse	7	181	4.61	18.1	30.63	6.05
Asc	22	1595	3.67	17.4	11.36	4.32
Fse	10	802	2.20	17.0	12.83	5.33

783

784

785

786

787

LIST OF FIGURES

788

789

790 Figure 1. Location of the study within the Amazon basin. The inset shows the
791 Geoscience Laser Altimeter System (GLAS) coverage (strings), airborne laser scanning
792 (ALS) data acquisition and the available field inventory plots across the Xingu basin.

793 Figure 2. Vegetation cover map adapted from IBGE (2004) in the left, and diagrams of
794 height estimates from ALS LiDAR data in the right, to illustrate structural variation
795 between the three predominant forest types in the study area (Dse, Asc and Fse). Each
796 Airborne Laser Scanning (ALS) plot represents an area of 100 m x100 m to describe the
797 heights in the three different forests.

798 Figure 3. Canopy volume models (CVMs) based on the Airborne Laser Scanning (ALS)
799 for (a) Dense ombrophilous forest (Dse); (b) Open ombrophilous Forest (Asc); and (c)
800 Semi-deciduous forest (Fse).

801 Figure 4. Seasonal profiles of GLAS-derived entropy for the three different forest types
802 of the study area. GLAS data were obtained only for the months indicated in the x-axis.
803 Just for reference, the shaded area represents the quarter when the Airborne Laser
804 Scanning (ALS) data were collected in 2012.

805 Figure 5. MODIS-derived anisotropy images during (a) March, (b) June and (c) October
806 of 2006 to illustrate seasonal and spatial changes in multi-angle reflectance across the
807 Xingu basin.

808 Figure 6. Relationship between MODIS-derived anisotropy and ALS-derived entropy
809 (or canopy roughness).

810 Figure 7. Relationship between MODIS-derived anisotropy and GLAS-derived entropy
811 using observations for (a) March, (b) June and (c) October of 2006.

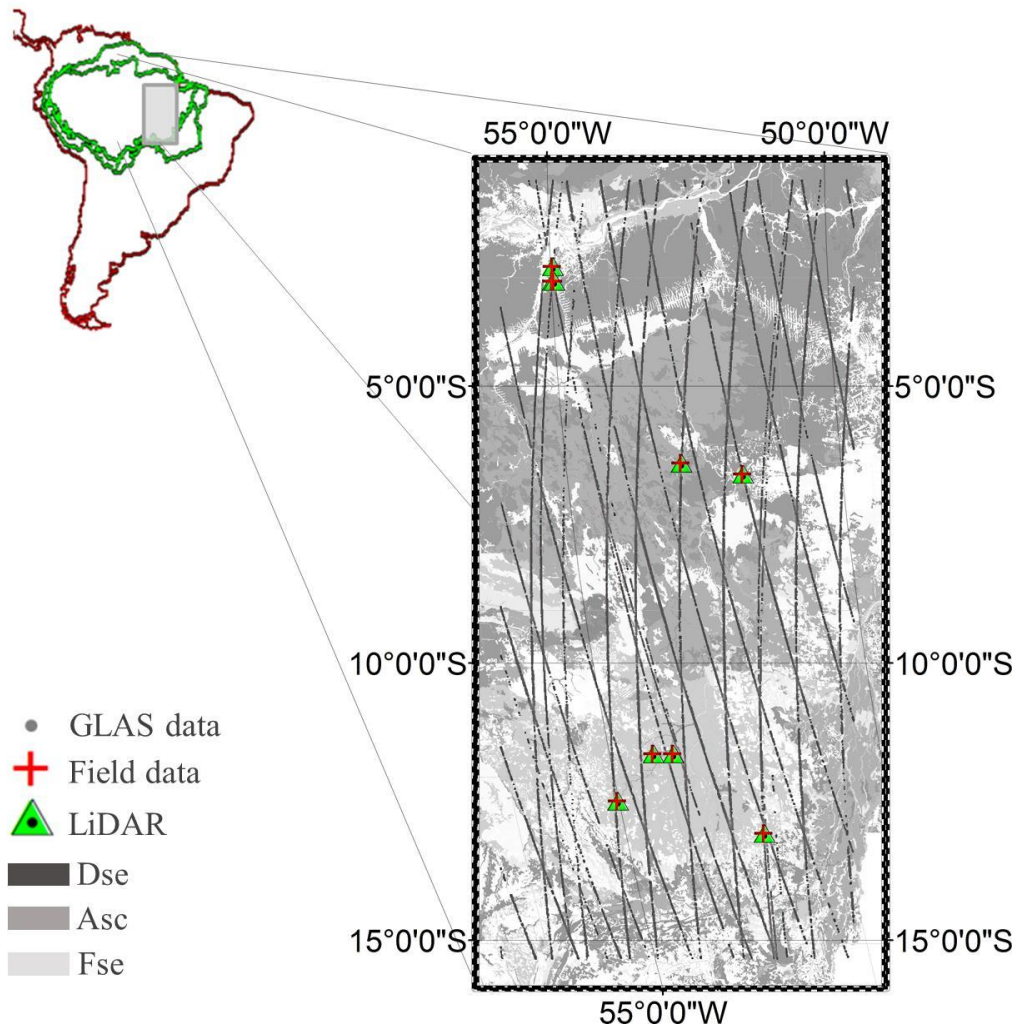
812 Figure 8. Relationship between MODIS-derived anisotropy and backscattering (σ^0)
813 measurements from SeaWinds/QSCAT over Amazonian tropical forests considering the
814 period 2001 to 2009.

815 Figure 9. Time series profiles of MODIS-derived (a) GLAS entropy estimated using the
816 regression model of Figure 7c, and (b) MODIS-derived SeaWinds/QuikSCAT
817 backscattering (σ^0) from the model of Figure 8. Results are shown as spatial average for
818 Dense (Dse) and Open (Asc) Ombrophilous Forests and the Semi-Deciduous Forest
819 (Fse) between 2000 and 2012 for the Xingu basin.

820

821 Figure A1. Comparison between MODIS-MAIAC EVI (normalized for directional
822 effects) and estimates of canopy entropy derived from ALS (a), GLAS (b) and
823 QuikSCAT (c). The vegetation index was significantly less suited to describe canopy
824 structural parameters than Anisotropy.

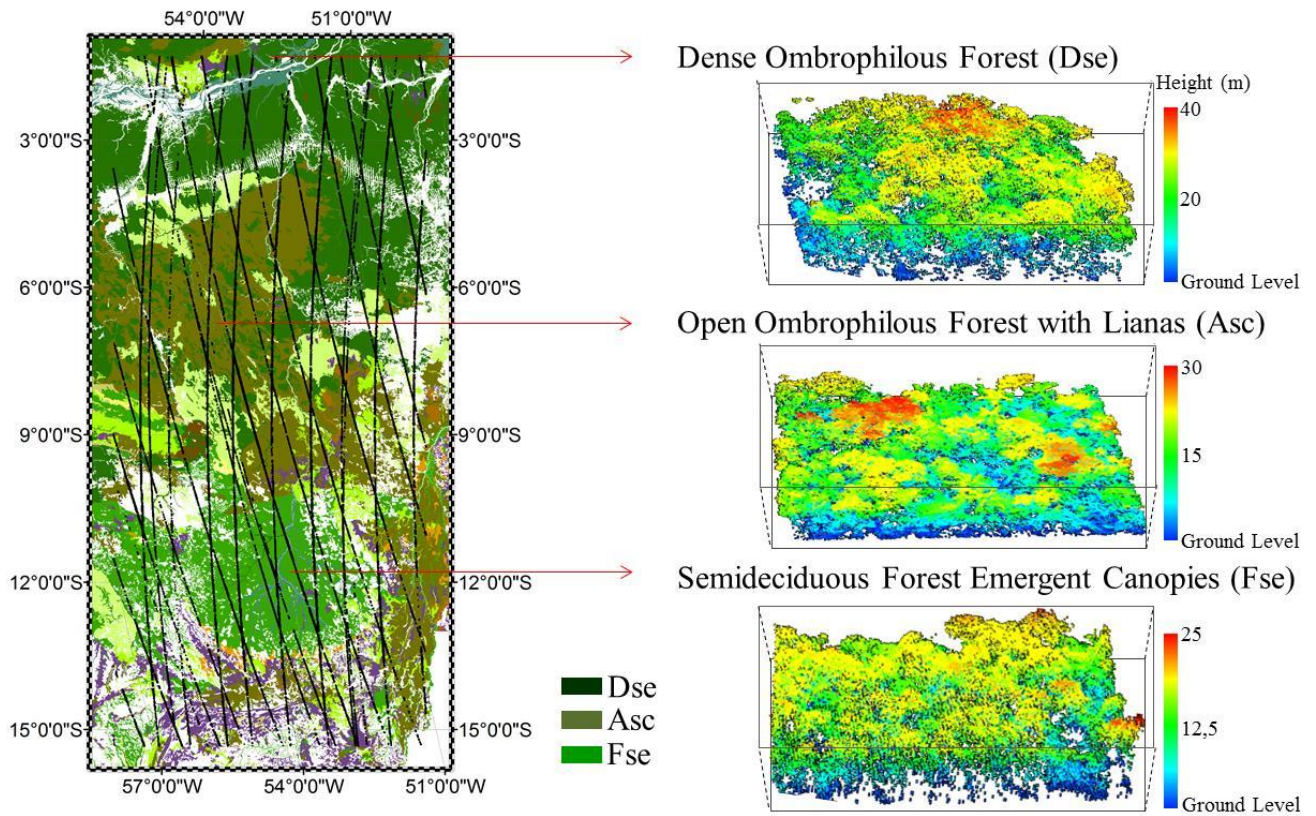
825



826

827 **Figure 1**

828



829

830 **Figure 2**

831

832

833

834

835

836

837

838

839

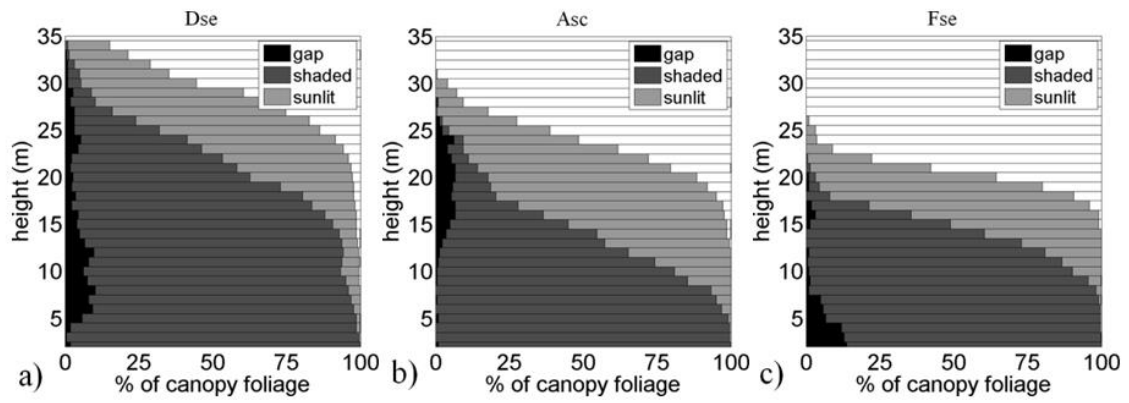
840

841

842

843

844



845

846 **Figure 3**

847

848

849

850

851

852

853

854

855

856

857

858

859

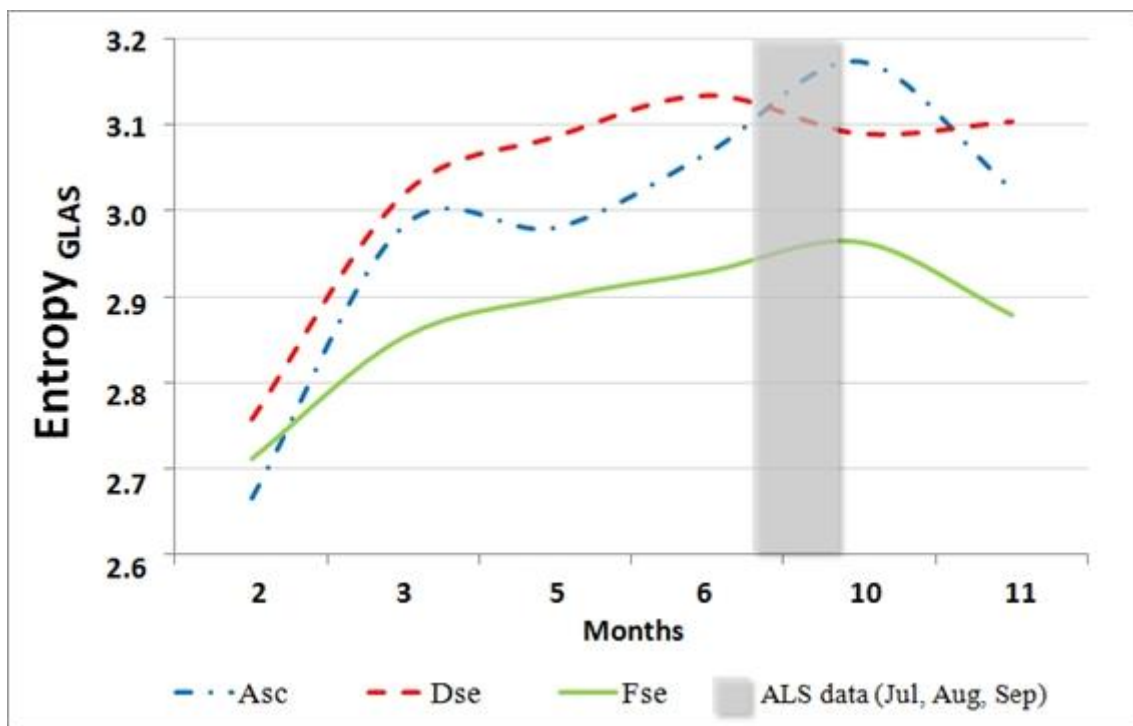
860

861

862

863

864



865

866 **Figure 4**

867

868

869

870

871

872

873

874

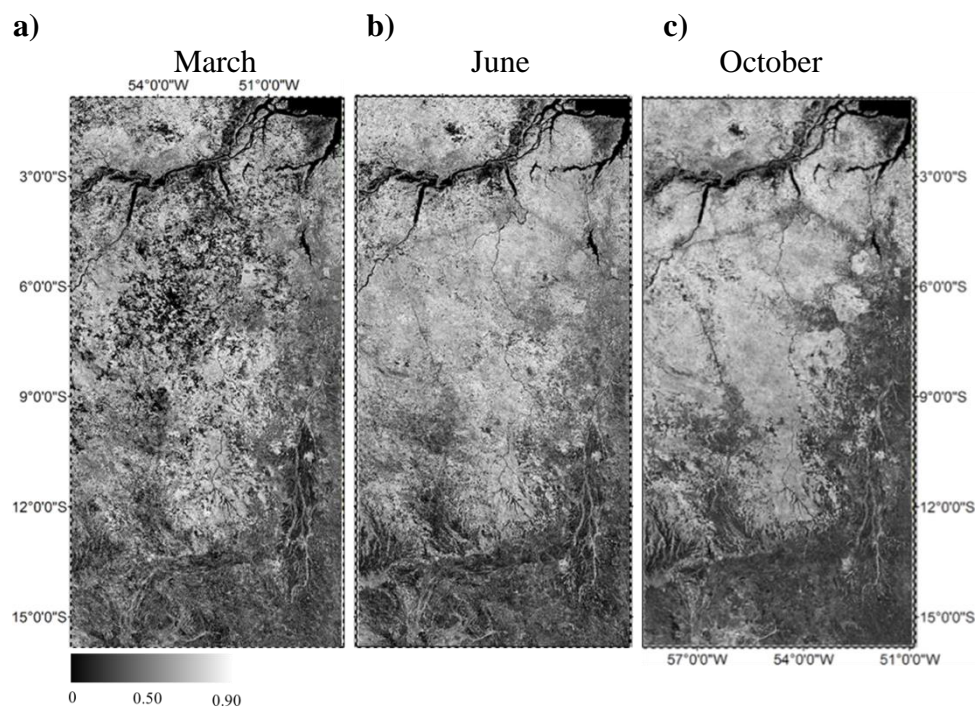
875

876

877

878

879



880 **Figure 5**

881

882

883

884

885

886

887

888

889

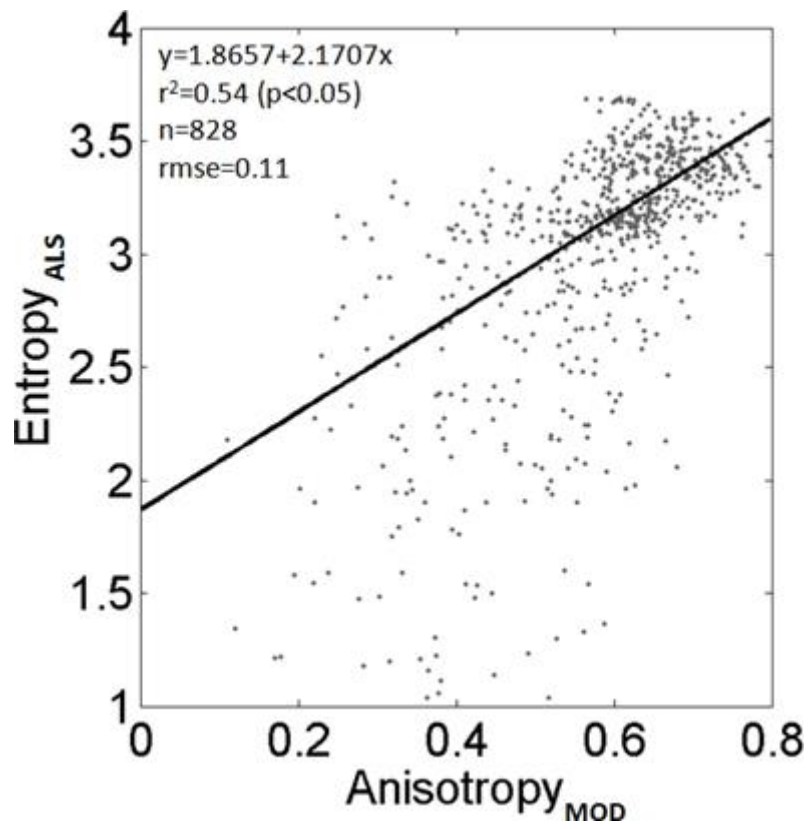
890

891

892

893

894



895

896 **Figure 6**

897

898

899

900

901

902

903

904

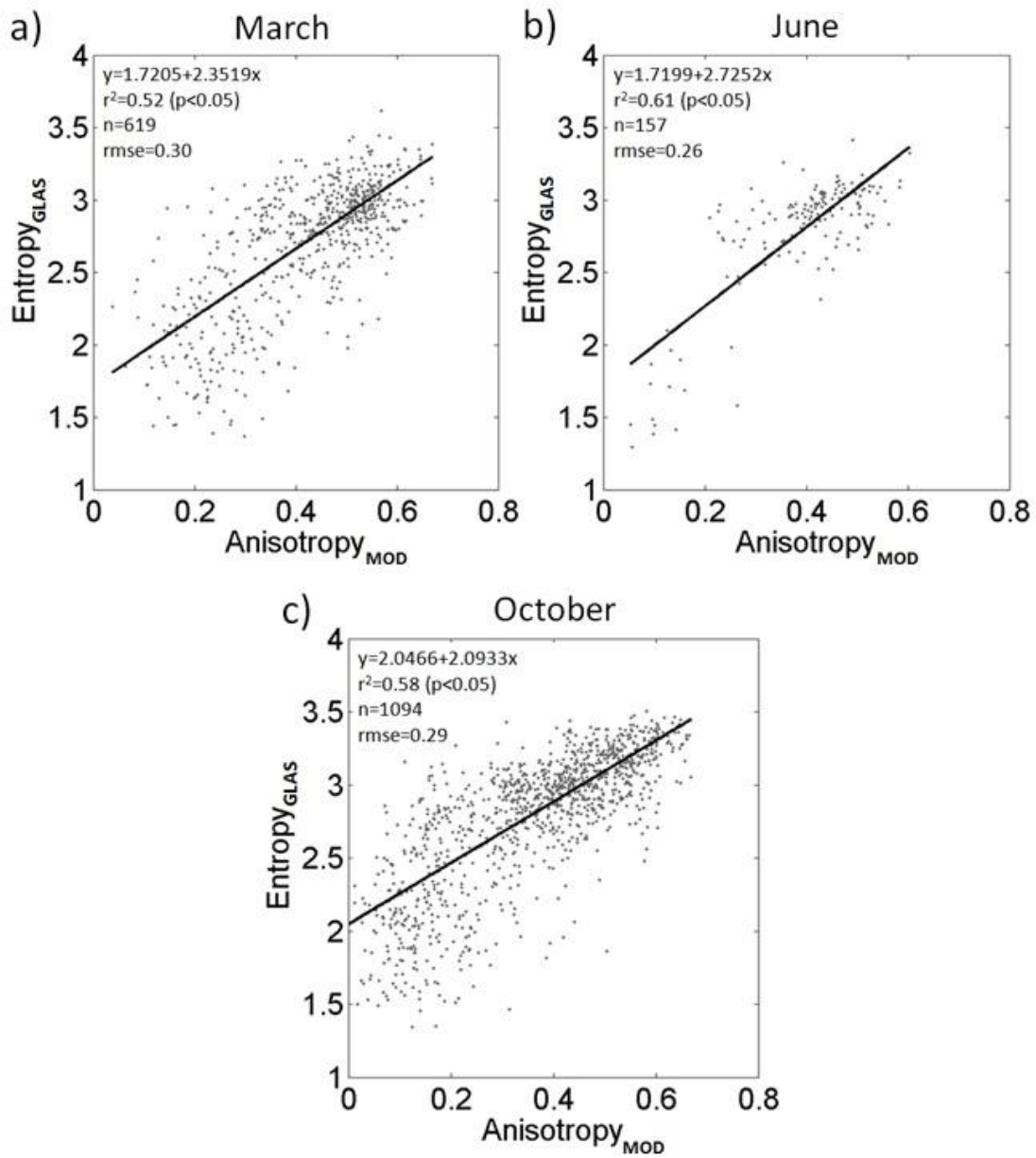
905

906

907

908

909



910

911 **Figure 7**

912

913

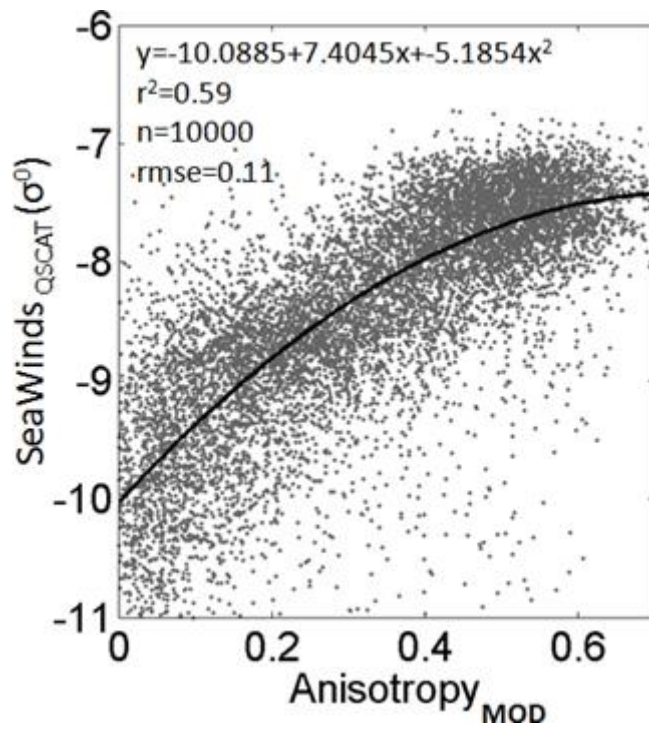
914

915

916

917

918



919

920 **Figure 8**

921

922

923

924

925

926

927

928

929

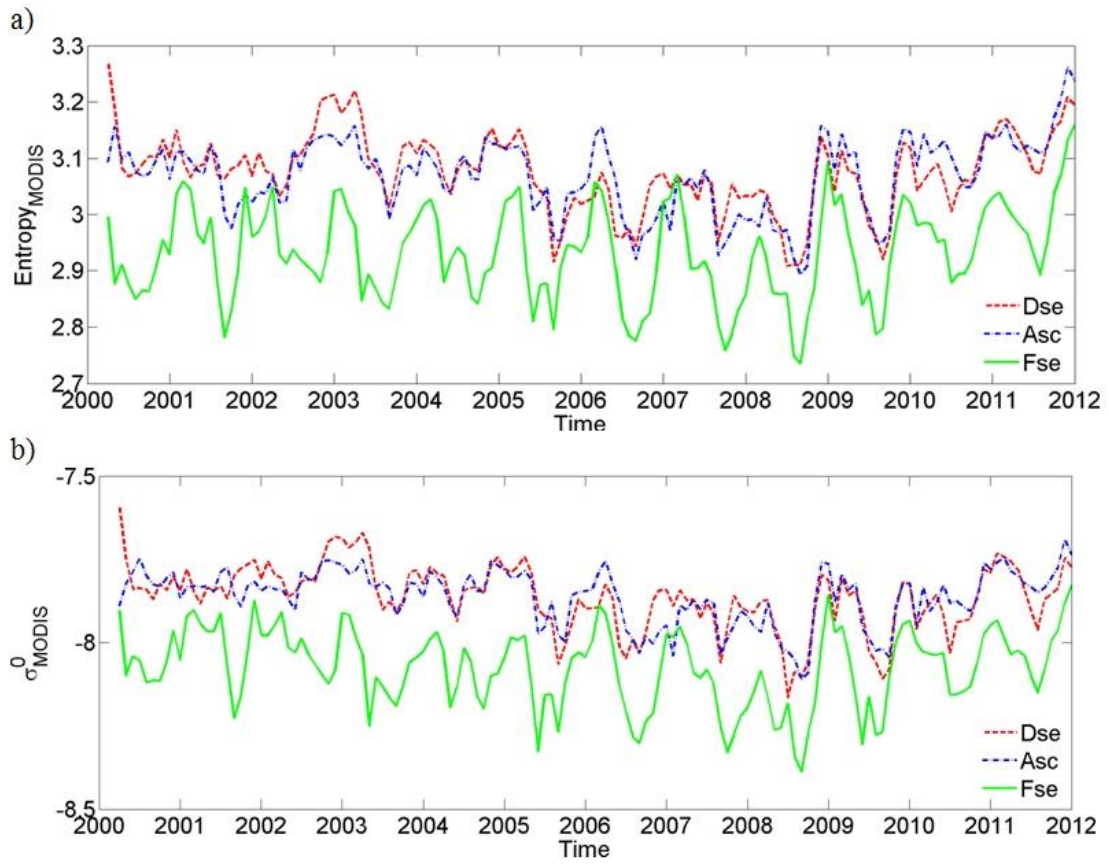
930

931

932

933

934



935

936 **Figure 9**

937

938

939

940

941

942

943

944

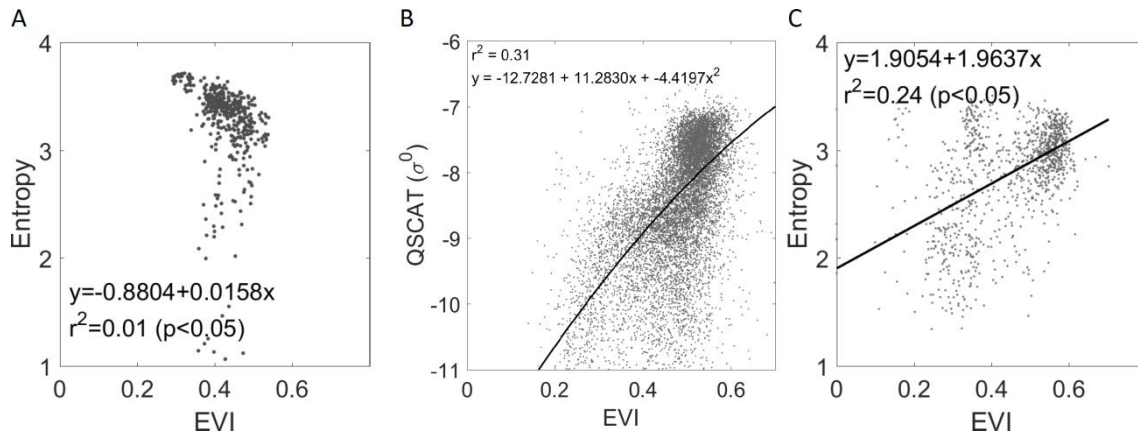
945

946

947

948 **APPENDIX A**

949



950

951 **Figure A1**

952

953